Laboratory-based x-ray dark-field microscopy

Michela Esposito,[1,*] Ian Buchanan,[1] Lorenzo Massimi,[1] Joseph D. Ferrara,[2] Paul R. Shearing,[3,4] Alessandro Olivo,[1] and Marco Endrizzi[1]

[1] *Department of Medical Physics and Biomedical Engineering, University College London, Malet Place, Gower Street, London WC1E 6BT, United Kingdom*

[2] *Rigaku Americas Corporation, 9009 New Trails Drive, The Woodlands, Texas 77381, USA*

[3] *Department of Chemical Engineering, Electrochemical Innovation Lab, University College London, London WC1E 7JE, United Kingdom*

[4] *The Faraday Institution, Quad One, Harwell Science and Innovation Campus, Didcot OX11 0RA, United Kingdom*

(Received 12 September 2022; revised 29 September 2023; accepted 12 December 2023; published 21 December 2023)

We demonstrate the capability of laboratory-based x-ray microscopes, using intensity-modulation masks, to access the submicron length scale in the dark-field contrast channel while maintaining micron resolution in the resolved (refraction and attenuation) channels. The dark-field contrast channel reveals the presence of ensembles of samples' features below the system resolution. Resolved refraction and attenuation channels provide multimodal high-resolution imaging down to the micron scale. We investigate the regimes of modulated and unmodulated dark field as well as refraction, quantifying their dependence on the relationship between feature size in the imaged object and aperture size in the intensity-modulation mask. We propose an analytical model to link the measured signal with the sample's microscopic properties. Finally, we demonstrate the relevance of the microscopic dark-field contrast channel in applications from both the life and physical sciences, providing proof-of-concept results for imaging collagen bundles in cartilage and dendritic growth in lithium batteries.

DOI: 10.1103/PhysRevApplied.20.064039

I. INTRODUCTION

In 1926 Slack, while studying refraction from prisms, noticed that x-ray beams were broadened when passing through graphite and hypothesized this was due to nonmeasurable internal refraction events from individual particles [1]. In this sense, small and ultrasmall angle x-ray scattering (SAXS and USAXS) or dark field, measuring multiple unresolved refraction events, provides a valuable tool to access information on sample features below the resolution of the imaging system. In fact, for phase-based imaging systems, the system spatial resolution sets the limit between the sample's frequency content that can be imaged directly and what is shown in the dark-field channel, as a result of multiple refraction events produced by ensembles of unresolved sample features. The complementarity between the resolved (attenuation and refraction) contrast channels and the unresolved dark field has been exploited in a number of applications, including pulmonary imaging [2–4], cancer detection [5], material science [6,7] and detection of threat materials [8]. Several phase-based imaging systems allow access to dark-field contrast, including analyzer-based imaging [9,10], grating interferometry [11,12], speckle-based imaging [13,14], propagation-based imaging [15], edge illumination [16], and beam tracking [17]. Dark field is retrieved using different strategies according to the different image formation principle underpinning the specific method, but it is generally associated with a blurring of the probe [18], represented, for example, by a reduction in visibility of the interference pattern in grating interferometry [19] or a broadening of the rocking curve in analyzer-based imaging [20].

This work is based on the use of an achromatic, incoherent, and noninterferometric imaging technique for the near field, relying on the use of intensity-modulation masks. Masks, consisting of an array of slits, shape the x-ray beam into an array of beamlets creating a structured illumination. Two different approaches can be used for sampling the resulting structured illumination: beam tracking (BT) [17,21] and edge illumination (EI) [16]. In BT, a

*michela.esposito@ucl.ac.uk

Published by the American Physical Society under the terms of the Creative Commons Attribution 4.0 International license. Further distribution of this work must maintain attribution to the author(s) and the published article's title, journal citation, and DOI.

high-resolution detector allows fine sampling of the structured beamlets, while in EI a second mask is placed at the detector position and translated transversely to sample the structured beamlets with a finer pitch than the detector pixel pitch. In both cases, sample properties are retrieved by evaluating intensity, position, and width of the shaped beamlets, with and without a sample in place.

Although visualization of submicron features in the dark-field contrast channel for mesoscale samples has been reported before [22–27], here we provide a demonstration of a laboratory setup accessing the submicron length scale in dark field while maintaining micron resolution in the resolved (refraction and attenuation) channels. In a multicontrast scenario, the resolution limit of the resolved channels is a key element in defining the fraction of sample features visualized directly at high resolution and complemented by ensemble information in dark field. Additionally, a modulated dark field, associated with the detection of individual features is also observed, further extending the applicability of this contrast channel beyond the conventional interpretation. We identify and discuss transition regions among length scales contributing to the refraction and modulated dark field versus dark field in its conventional (unmodulated) interpretation. We provide two examples of applications in the life and physical sciences, using x-ray energies spanning from 8 to 40 keV, for the detection of ensembles of sample features in the submicron length scale.

II. DARK-FIELD MODEL

The image formation principle associated with BT and EI is schematically shown in Fig. 1 while a detailed description of the experimental setup can be found in the Sec. III. X ray where beamlets, shaped by an intensity-modulation mask, are attenuated by a homogeneous sample, refracted when the phase gradient of the x-ray wave emerging from the sample is nonzero (as at the edges of the sample, for example), or broadened from the multiple refraction events arising from unresolved sample features. Experimentally acquired images of individual beamlets are shown in (b)–(c) (red boxes) a localized reduction of intensity (transmission), a lateral shift (refraction) and broadening (dark field), compared to reference beamlets (blue boxes). The shaped beamlets can be empirically modeled as the convolution of the mask aperture and the source projected focal spot [16] resulting in bell-shaped curves. A Gaussian distribution often represents a good approximation for the shaped beamlets, as a result of a Gaussian distribution of the focal spot. Here we provide an analytical model for the measured dark-field signal through the Fokker-Planck equation of paraxial wave optics [28], an extension to the transport-of-intensity equation [29], including diffusive effects associated with dark field. The evolution of a complex paraxial scalar wave field, propagating along the optical axis z can be described as

$$\frac{\partial I(x,z)}{\partial z} = -\frac{1}{k}\frac{\partial}{\partial x}\left[I(x)\frac{\partial \phi_s(x)}{\partial x}\right] + \frac{\partial^2}{\partial x^2}\left[D(x,z)I(x,z)\right], \tag{1}$$

where the phase of the wave field emerging from the sample in its exit plane $\phi(x, z = 0)$ has been decomposed [30] into slow- and fast-varying phase components $\phi(x, z = 0) = \phi_s(x) + \phi_f(x)$. The former is responsible for phase-contrast effects arising from the Laplacian of the phase (propagation-based imaging) or the gradient of the phase (differential phase-contrast imaging). The latter includes fluctuations that are fast varying on the length scale at which the signal is sampled (i.e., the mask aperture), and it is expressed through the diffusion coefficient D, responsible for angular dispersion effects associated with the USAXS fan. Assuming that refraction effects can be neglected, as far as $\phi_f(x)$ is concerned, and that D is slowly varying in x over the sampling width (mask aperture), so it can be moved out of the Laplacian [31], Eq. (1) becomes

$$\frac{\partial I(x,z)}{\partial z} = D\frac{\partial^2 I(x,z)}{\partial x^2}, \tag{2}$$

where the explicit dependency of D on z has been omitted for simplicity's sake. In BT or EI, a shaped beamlet centred on zero along the transverse axis x and with width σ, can be described by a Gaussian function [16,17] $I(x) = \frac{1}{\sqrt{2\pi}\sigma}e^{\frac{-x^2}{2\sigma^2}}$, which substituted into Eq. (2) gives

$$\frac{\partial I(x,z)}{\partial z} = D\left[\frac{x^2-\sigma^2}{\sigma^4}\right]I(x). \tag{3}$$

By solving Eq. (3) we obtain

$$I(x,z) = I(x)e^{-Dz\left[\frac{\sigma^2-x^2}{\sigma^4}\right]}. \tag{4}$$

Writing explicitly the first term on the right-hand side of Eq. (4) with the variable substitution:

$$\sigma_s^2 = \frac{\sigma^4}{\sigma^2 - 2Dz}, \tag{5}$$

Equation (4) becomes

$$I(x,z) = \frac{e^{-\left[\frac{Dz}{\sigma^2}\right]}}{\sqrt{2\pi}\sigma}e^{\left[-\frac{x^2}{2\sigma_s^2}\right]}. \tag{6}$$

Equations (5) and (6) show that, up to a multiplicative factor, a scattered beam is still Gaussian, with variance given by σ_s^2. For a nonscattering sample ($D = 0$) or for contact imaging ($z = 0$) $\sigma_s^2 = \sigma^2$, while increasing D or z leads

to a broadening of the beamlets. Equation (5) is subject to the validity condition $\sigma^2 > 2Dz$. It is of note that Eq. (6), derived from a continuity equation [Eq. (1)], and within the limits of our experiments, i.e., near-field approximation, it is to be intended as expressing energy conservation regardless of its explicit dependence on z. In fact, it can be shown that the integral along the x direction of the intensity of the scattered beamlet from Eq. (6) is constant at all z, within the limits of the near-field approximation. Analogous equations, also with an explicit z dependence, are reported in Refs. [31] and [32]. We can link the diffusion coefficient D to the sample microscopic properties by using the relationship $D = \theta^2 z$ [28], where θ is the opening angle of the USAXS. The USAXS fan can also be considered the result of the incoherent superposition of unresolvable refraction events, with angular distribution given by ϕ_f'/k. This approximation allows linking the USAXS fan to the fast-varying phase component of a scattering sample $\theta^2 \approx \mathrm{var}(\phi_f'/k)$ [33]. Therefore, Eq. (6) establishes a relationship between measured beamlet width and phase. A reference beamlet and the effect of USAXS modeled using Eq. (6), is shown in Fig. 1(e).

III. METHODS

A. Experimental setup

Two different experimental setups were used for this work. Phantom studies and cartilage imaging were performed using a BT microscope, while, due to different samples' requirements, battery imaging was performed using an EI system. For the BT microscope [21], a monochromatic x-ray beam (8 keV), produced by a rotating copper anode x-ray source and focused to a 350-μm focal spot by double-curved multilayer optics, was shaped by a free-standing gold mask with 2-μm apertures and a 20-μm period. The shaped beamlets were sampled by a custom-built indirect detector with 1.1-μm pixel pitch, placed 15-mm downstream of the sample [Fig. 1(a)], at a unitary geometrical magnification.

A higher energy source (an 80-kVp tungsten spectrum with average energy of approximately equal to 40 keV) was employed for the EI system [34]. To combine small mask apertures (3 μm, 20-μm period) with a high-efficiency detector (Hamamatsu C9732DK with a 50-μm pixel), a highly magnified geometry was adopted. A detector mask (pitch 98-μm, aperture 29 μm) was translated transversally to offer an effective pixel size smaller than the detector pixel pitch. Presample and detector masks were placed at 13 and 130 cm from the source, respectively. The use of a 10× magnification imposed the use of a microfocal source (approximately equal to 5-μm focal spot).

B. Retrieval

In both experimental setups, samples were translated orthogonally to the mask apertures by a quantity equal to the mask period (20 μm), in steps equal to the Nyquist frequency associated with the mask aperture width. Images were acquired at each step and recombined, after retrieval, in a process dubbed *dithering* [35]. Dithering allows for the aperture-limited resolution demonstrated in Refs. [21,36]. The retrieval of transmission (T), refraction (R) and dark field (DF) was obtained by evaluating (A_s, μ_s, σ_s^2) and (A_r, μ_r, σ_r^2) namely amplitude, mean, and variance of the structured beamlets with and without a sample in place. Contrast channels were retrieved as follows:

$$T = \frac{A_s}{A_r}, \tag{7}$$

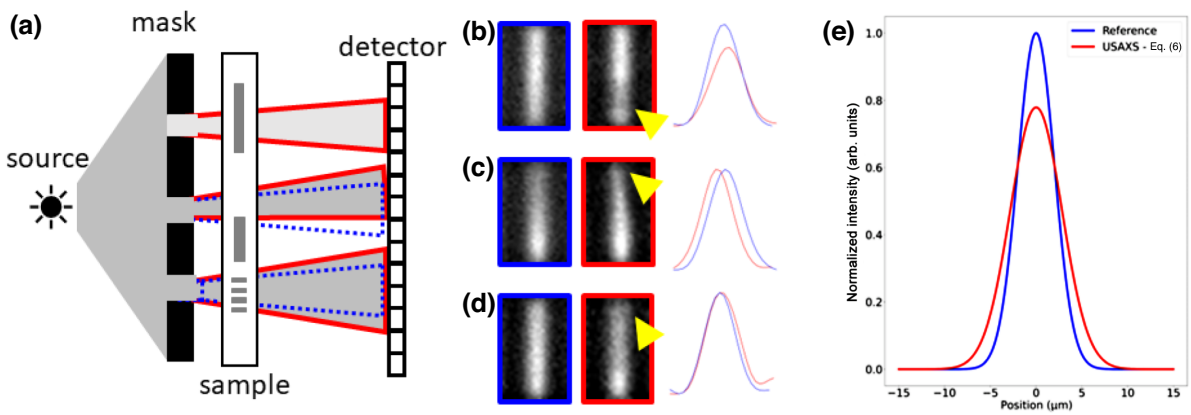

FIG. 1. (a) Image formation principle in BT and EI (figure not to scale). Note that an additional mask, placed at the detector position is needed in EI, as discussed in Sec. III. Changes in the shaped beamlet with (red) and without (blue) a sample are schematically shown. Images of a single aperture and the effects of transmission (b), refraction (c), and dark field (d), namely a reduction of intensity, a lateral shift and a broadening of the beamlet, respectively, are displayed and highlighted by a yellow arrowhead. (e) A reference beamlet (a Gaussian with width $\sigma = 2$ μm) and the effect of USAXS modeled using Eq. (6).

$$R = \frac{\mu_s - \mu_r}{z}, \tag{8}$$

$$\mathrm{DF} = \frac{\sigma_s^2 - \sigma_r^2}{z^2}, \tag{9}$$

where z is the sample to detector distance.

C. Samples

To quantify refraction and dark field at different length scales, two bar patterns consisting of Au bars on a SiN_3 membrane were imaged with the BT system. Bar width varied between 100 nm and 5 μm with an accuracy of 1%. Two different bar thicknesses were used for this work: 500 and 1000 nm. Additionally, the BT microscope was used to image rabbit articular cartilage. A < 1-mm-thick slice was imaged in air. A symmetrical lithium electrochemical cell was also imaged using the EI system. The electrochemical cell was obtained by forming Li electrodes around a Cu wire, placed in a 1-mm diameter Kapton tube. The space between the two electrodes was filled with liquid electrolytes [37]. A schematic of the cell, adapted from Ref. [37] is shown in Fig. 5(a). The cell was plated using a constant current of 1 $\mathrm{mA/cm^2}$.

IV. RESULTS AND DISCUSSION

A. Refraction to dark-field transition

Figure 2 shows refraction (a) and dark-field (b) images for Au bars with feature sizes of 1000, 500, and 250 nm as imaged with the BT microscope, and corresponding intensity profiles in (c) and (d). As expected from theoretical [38] and experimental [21] results, individual 1-μm-wide bars can still be identified in the refraction channel (c), consistently with the spatial resolution being limited by the mask aperture width. The dark-field signal at this length scale appears modulated with positive and negative peaks corresponding to broadening and narrowing of the shaped beamlets (see Ref. [21] and Supplemental Material therein), allowing identification of individual features. At the submicron length scale, individual bars cannot be resolved in the refraction channel, as expected. However, an unmodulated and positive (broadening of the beamlets) dark-field signal can be associated with them [see 500- and 250-nm bars in Fig. 2(b)]. As the bar width decreases from 500 to 250 nm, the intensity of the dark-field signal increases as a result of increasing density of scatterers. This shows that the x-ray microscope can access submicron length scales using the dark-field channel for features' ensembles, while refraction and the modulated dark field resolve length scales comparable to and larger than the aperture size.

To obtain a numerical description of these findings, simulated data obtained from Fresnel-Kirchhoff integrals [39] were retrieved with the same algorithm used for the experimental images. Amplitude of refraction (A_r) and dark field (A_{DF}) were calculated where a modulation in the dark-field signal could be observed. For a modulated signal S, amplitude is given by $A_S = \overline{\max[S(i)] - \min[S(i)]}$, where the bar indicates average over the pairs i of positive and negative peaks. The average dark field ($\mathrm{DF_{av}}$) over a region

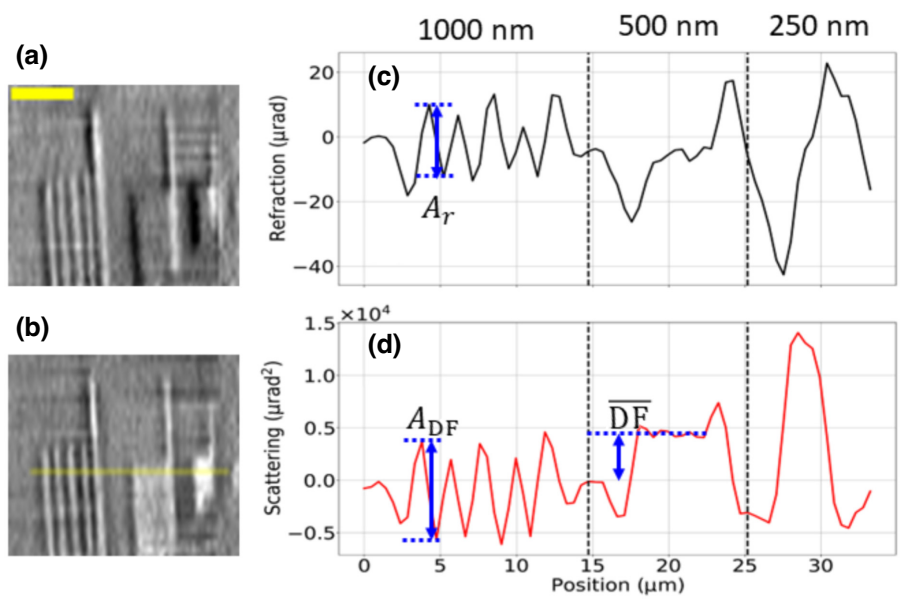

FIG. 2. Refraction (a) and dark-field (b) images of bar patterns with 1000-, 500-, and 250-nm half-periods and relevant intensity profiles in (c),(d) (scale bar 10 μm) A visual depiction of the location of the line out is shown in (b). Amplitude of refraction (A_r) and modulated dark field (A_{DF}) are displayed alongside the average dark field ($\mathrm{DF_{av}}$).

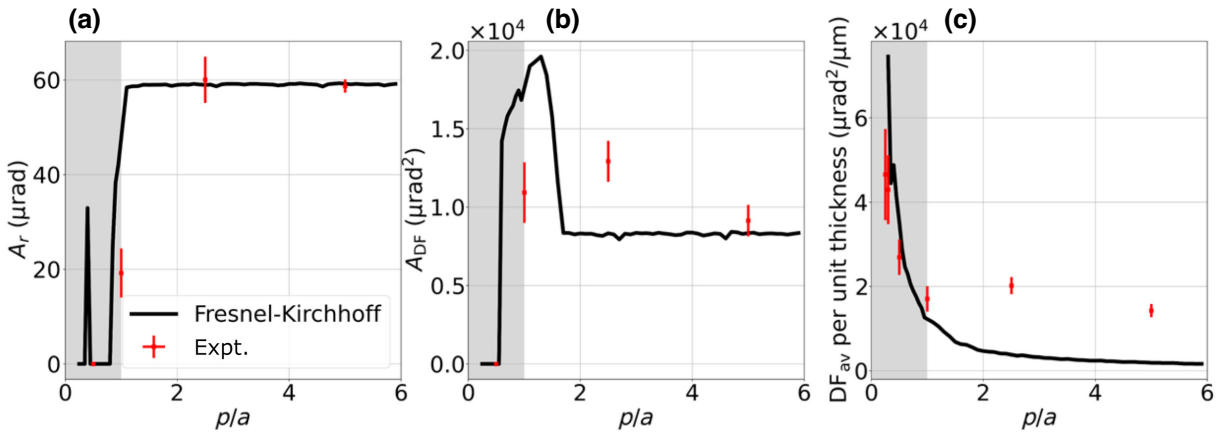

FIG. 3. Retrieved refraction amplitude (a), dark-field amplitude (b), and average dark field per unit thickness (c) as a function of the ratio between bar pattern period and mask aperture (p/a). Solid line and red squares are obtained by retrieval of synthetic data from Fresnel-Kirchhoff simulations and experimental data, respectively. The shadowed areas highlight a ratio of pattern period to aperture smaller than one, i.e., of unresolvable features.

of interest (see Fig. 2) was also calculated and normalized by bar thickness to allow comparing points from bar patterns of different thicknesses. It is of note that the numerical model was computed using nominal period and thickness for the bar patterns. Sample thickness was convolved with a narrow Gaussian (0.5-μm width) to avoid unrealistically sharp edges. A small uncertainty (approximately equal to 1%) is expected on the bars' period, but a significantly larger one, although unknown, is assumed for the thickness, due to the uncertainties associated with the manufacturing process.

While A_r and A_{DF} are linked to the capability of resolving individual features with positive and negative peaks, respectively, DF_{av} corresponds to the common interpretation of dark field, namely the detection of ensembles of sample's features below the resolution limit of the instrument. Figure 3 compares the experimentally measured A_r (a), A_{DF} (b), and DF_{av} per unit thickness (panel c) with the corresponding values retrieved from the Fresnel-Kirchhoff model (solid line), as a function of the ratio (p/a) of bar pattern period to mask aperture size.

A_r is constant for $p/a \geq 1$, decreases sharply for $p/a < 1$ [shaded area of Fig. 3(a)]. This is consistent with a resolution limited by the mask aperture width [21]. At small periods, ($p/a \approx 0.4$) an isolated peak is observed, corresponding to a modulation of A_r smaller than that observed in the plateau region. This is due to aliasing, arising from sampling the simulated data at frequencies higher than the Nyquist frequency; the peak is observed at a frequency matching the second post-Nyquist lobe of the Fourier transform of the (square) aperture.

A_{DF} [Fig.3(b)] also exhibits a plateau for larger feature sizes and increases for $p/a < 2$. This arises from the summation of positive dark-field peaks inside the bars and

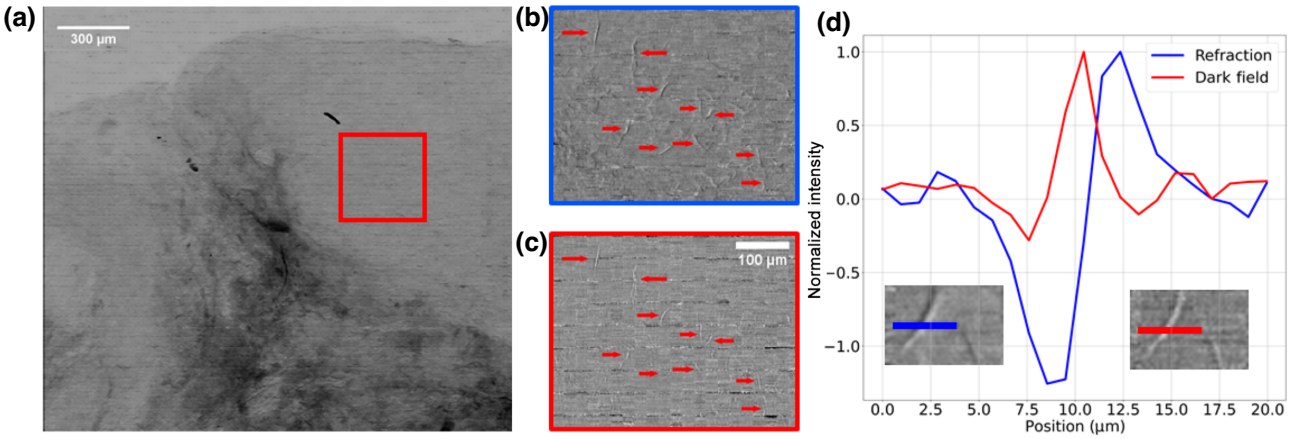

FIG. 4. (a) Transmission image of a slice of rabbit articular cartilage. (b),(c) Refraction and dark-field images for the region of interest highlighted in (a). Red arrows indicate collagen bundles. (d) Intensity profiles of retrieved refraction (blue) and dark field (red) for one of the bundles.

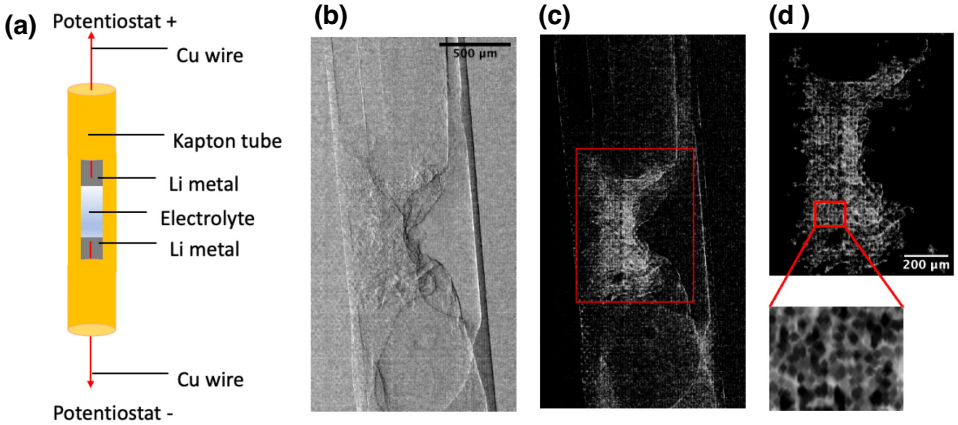

FIG. 5. (a) Schematic diagram of the lithium-lithium electrochemical cell, adapted from Ref. [37]. Retrieved refraction (b) and dark-field (c) images. (d) Segmentation of the area of high dark-field signal [corresponding to the red box of (c)], with a magnified view of a region of interest highlighting the presence of microstructures within the dark-field signal.

negative peaks outside them (see Ref. [21] and Supplemental Materials therein) when the bar width approaches the sampling size. For $p/a < 1$ A_{DF} decreases with a similar slope to A_r. The peak observed in simulations for $p/a < 2$ is not reproduced in the experimental data. This can be explained by accounting for the large uncertainty on bar thickness (see Sec. III) as well as for the sparse sampling of the experimental data, compared to the peak width. The first zero of A_r and A_{DF} are achieved at $p/a = 0.8$ and $p/a = 0.5$, respectively. This indicates that A_{DF} provides an increased contrast for smaller features, compared to A_r.

$\mathrm{DF_{av}}$ [Fig. 3(c)] plateaus to a constant value for large p/a ratios. The marked increase for $p/a < 1$ shows how the dark-field signal rises for ensembles of features below the system's resolution, providing a tool for revealing the presence of ensembles of unresolved features, in the submicron range at the resolution of this microscope. The aperture width represents a characteristic length that defines the transition between phase gradient-based contrast (A_r and A_{DF}) and unmodulated dark field ($\mathrm{DF_{av}}$). This is analogous to what was reported for grating interferometry and speckle-based imaging, where the same transition is driven by autocorrelation length [27,40] and speckle size [41], respectively. While a quantitative comparison between experimental and theoretical data of Fig. 3 cannot be drawn, mainly due to large uncertainties on bar thicknesses, we observe a qualitative agreement in the trends followed by the two datasets.

B. Applications in Physical and Life Sciences

In the following, we apply the method's ability to identify sub-micron features to applications in the life and physical sciences. The retrieved transmission image of a cartilage slice is shown in Fig. 4(a), using the same 8-keV BT system used for the bar pattern experiments. A magnified view of the region-of-interest (red square in panel a) is shown for the retrieved refraction and dark field signals in panels (b) and (c), respectively. Both images feature fibre-like structures, highlighted by red arrows. Panel (d) shows normalised intensity profiles of both channels, for the fibre shown in the insets. Refraction (blue), proportional to differential phase, exhibits a positive and a negative peak, while the dark field (red) shows a sharp positive maximum between the refraction peaks. Overall, the $\approx 5-6$ μm fibre is resolved by the system, and its outer boundaries correspond to the refraction peaks. However, collagen fibres are hierarchical structures, with the first sub-structure consisting of fibrils in the hundreds of nanometres range, generating the sharp central peak in the dark field signal.

The 40-keV EI setup (see Sec. III) was used to image a lithium-lithium electrochemical cell. The retrieved refraction and dark-field images of the lithium-lithium electrochemical cell are shown in Figs. 5(b) and 5(c), respectively. While refraction detects the outlines of the cell components, the dark-field image features a strong signal increase in the central area between the electrodes. This suggests the presence of subresolution features consistent with the creation of Li moss and high surface area lithium (HSAL) at the electrodes, as shown in Ref. [37]. The region corresponding to the red box in (c) is shown in (d) after segmentation, alongside a magnified view of a small region of interest. The heterogeneity of the dark-field signal suggests the presence of different size microstructures forming at the electrodes, consistent with the complex morphology of dendritic lithium formed during electroplating.

V. CONCLUSIONS

We have demonstrated how x-ray microscopes based on intensity-modulation masks, either in BT or EI configuration, can detect ensembles of submicron features

in the dark-field contrast channel while providing complementary high-resolution images with micron resolution. The applications discussed in this paper demonstrate how the dark-field contrast channel, combined with a high-resolution imaging, can facilitate the identification of complex structures with submicron features (collagen bundles and dendritic growth) beyond the resolution limit of the instrument. The analytical model developed in this work allows one linking the measured dark-field signal to the sample's microscopic properties. This is of interest for imaging of hierarchical structures, e.g., collagen bundles and fibrils, which span across different length scales. Future development could allow this model to be used to quantify feature size of the sample's scattering allowing a quantitative interpretation of the dark-field channel.

ACKNOWLEDGMENTS

Research reported in this publication was supported by the National Institute of Biomedical Imaging and Bioengineering of the National Institutes of Health under Award No. R01EB028829. The content is solely the responsibility of the authors and does not necessarily represent the official views of the National Institutes of Health. Additional support was received from the EPSRC (Grants No. EP/T005408/1, No. EP/P023231/1, and No. EP/M028100/1), the Wellcome Trust 221367/Z/20/Z, and the European Union's Horizon 2020 research and innovation programme under Grant Agreement No. 777222. A.O. and P.R.S. were supported by the Royal Academy of Engineering under their "Chairs in Emerging Technologies" scheme (CiET1819/2/78 and CiET1718/59, respectively).

[1] C. M. Slack, The refraction of x-rays in prisms of various materials, Phys. Rev. **27**, 691 (1926).

[2] F. T. Gassert, T. Urban, M. Frank, K. Willer, W. Noichl, P. Buchberger, R. Schick, T. Koehler, J. von Berg, A. A. Fingerle, A. P. Sauter, M. R. Makowski, D. Pfeiffer, and F. Pfeiffer, X-ray dark-field chest imaging: Qualitative and quantitative results in healthy humans, Radiology **301**, 389 (2021), publisher: Radiological Society of North America.

[3] P. Modregger, T. P. Cremona, C. Benarafa, J. C. Schittny, A. Olivo, and M. Endrizzi, Small angle x-ray scattering with edge-illumination, Sci. Rep. **6**, 30940 (2016).

[4] A. Yaroshenko, K. Hellbach, M. Bech, S. Grandl, M. F. Reiser, F. Pfeiffer, and F. G. Meinel, Grating-based X-ray dark-field imaging: A new paradigm in radiography, Curr Radiol Rep **2**, 57 (2014).

[5] K. Scherer, A. Yaroshenko, D. A. Bölükbas, L. B. Gromann, K. Hellbach, F. G. Meinel, M. Braunagel, J. v. Berg, O. Eickelberg, M. F. Reiser, F. Pfeiffer, S. Meiners, and J. Herzen, X-ray dark-field radiography – in-vivo diagnosis of lung cancer in mice, Sci. Rep. **7**, 402 (2017), number: 1 Publisher: Nature Publishing Group.

[6] D. Shoukroun, L. Massimi, F. Iacoviello, M. Endrizzi, D. Bate, A. Olivo, and P. Fromme, Enhanced composite plate impact damage detection and characterisation using x-ray refraction and scattering contrast combined with ultrasonic imaging, Compos. Part B: Eng. **181**, 107579 (2020).

[7] F. Prade, K. Fischer, D. Heinz, P. Meyer, J. Mohr, and F. Pfeiffer, Time resolved x-ray dark-field tomography revealing water transport in a fresh cement sample, Sci. Rep. **6**, 29108 (2016).

[8] T. Partridge, A. Astolfo, S. S. Shankar, F. A. Vittoria, M. Endrizzi, S. Arridge, T. Riley-Smith, I. G. Haig, D. Bate, and A. Olivo, Enhanced detection of threat materials by dark-field x-ray imaging combined with deep neural networks, Nat. Commun. **13**, 4651 (2022).

[9] L. Rigon, H.-J. Besch, F. Arfelli, R.-H. Menk, G. Heitner, and H. Plothow-Besch, A new DEI algorithm capable of investigating sub-pixel structures, J. Phys. D: Appl. Phys. **36**, A107 (2003).

[10] T. J. Davis, D. Gao, T. E. Gureyev, A. W. Stevenson, and S. W. Wilkins, Phase-contrast imaging of weakly absorbing materials using hard x-rays, Nature **373**, 595 (1995).

[11] F. Pfeiffer, M. Bech, O. Bunk, T. Donath, B. Henrich, P. Kraft, and C. David, X-ray dark-field and phase-contrast imaging using a grating interferometer, J. Appl. Phys. **105**, 102006 (2009).

[12] A. Malecki, G. Potdevin, T. Biernath, E. Eggl, K. Willer, T. Lasser, J. Maisenbacher, J. Gibmeier, A. Wanner, and F. Pfeiffer, X-ray tensor tomography(a), Europhys. Lett. **105**, 38002 (2014).

[13] S. Berujon and E. Ziegler, Near-field speckle-scanning-based x-ray imaging, Phys. Rev. A **92**, 013837 (2015).

[14] H. Wang, Y. Kashyap, and K. Sawhney, From synchrotron radiation to lab source: Advanced speckle-based x-ray imaging using abrasive paper, Scientific Reports **6**, 20476 (2016), number: 1 Publisher: Nature Publishing Group.

[15] T. E. Gureyev, D. M. Paganin, B. Arhatari, S. T. Taba, S. Lewis, P. C. Brennan, and H. M. Quiney, Dark-field signal extraction in propagation-based phase-contrast imaging, Phys. Med. Biol. **65**, 215029 (2020), publisher: IOP Publishing.

[16] M. Endrizzi, P. C. Diemoz, T. P. Millard, J. Louise Jones, R. D. Speller, I. K. Robinson, and A. Olivo, Hard x-ray dark-field imaging with incoherent sample illumination, Appl. Phys. Lett. **104**, 024106 (2014).

[17] F. A. Vittoria, G. K. N. Kallon, D. Basta, P. C. Diemoz, I. K. Robinson, A. Olivo, and M. Endrizzi, Beam tracking approach for single-shot retrieval of absorption, refraction, and dark-field signals with laboratory x-ray sources, Appl. Phys. Lett. **106**, 224102 (2015).

[18] Y. I. Nesterets, On the origins of decoherence and extinction contrast in phase-contrast imaging, Opt. Commun. **281**, 533 (2008).

[19] F. Pfeiffer, M. Bech, O. Bunk, P. Kraft, E. F. Eikenberry, C. Brönnimann, C. Grünzweig, and C. David, Hard-x-ray dark-field imaging using a grating interferometer, Nat. Mater **7**, 134 (2008).

[20] M. N. Wernick, O. Wirjadi, D. Chapman, Z. Zhong, N. P. Galatsanos, Y. Yang, J. G. Brankov, O. Oltulu, M. A. Anastasio, and C. Muehleman, Multiple-image radiography, Phys. Med. Biol. **48**, 3875 (2003).

[21] M. Esposito, L. Massimi, I. Buchanan, J. D. Ferrara, M. Endrizzi, and A. Olivo, A laboratory-based, low-energy, multi-modal *x*-ray microscope with user-defined resolution, Appl. Phys. Lett. **120**, 234101 (2022).

[22] B. C. Larson, W. Yang, G. E. Ice, J. D. Budai, and J. Z. Tischler, Three-dimensional *x*-ray structural microscopy with submicrometre resolution, Nature **415**, 887 (2002).

[23] B. K. Blykers, C. Organista, M. N. Boone, M. Kagias, F. Marone, M. Stampanoni, T. Bultreys, V. Cnudde, and J. Aelterman, Tunable *x*-ray dark-field imaging for sub-resolution feature size quantification in porous media, Sci. Rep. **11**, 18446 (2021).

[24] Y. Y. How, D. M. Paganin, and K. S. Morgan, On the quantification of sample microstructure using single-exposure *x*-ray dark-field imaging via a single-grid setup, Sci. Rep. **13**, 11001 (2023).

[25] T. H. Jensen, M. Bech, O. Bunk, T. Donath, C. David, R. Feidenhans'l, and F. Pfeiffer, Directional *x*-ray dark-field imaging, Phys. Med. Biol. **55**, 3317 (2010).

[26] T. Thuering, P. Modregger, T. Grund, J. Kenntner, C. David, and M. Stampanoni, High resolution, large field of view *x*-ray differential phase contrast imaging on a compact setup, Appl. Phys. Lett. **99**, 041111 (2011).

[27] F. Prade, A. Yaroshenko, J. Herzen, and F. Pfeiffer, Short-range order in mesoscale systems probed by *x*-ray grating interferometry, EPL (Europhysics Letters) **112**, 68002 (2015).

[28] D. M. Paganin and K. S. Morgan, *X*-ray Fokker–Planck equation for paraxial imaging, Sci. Rep. **9**, 17537 (2019).

[29] M. R. Teague, Deterministic phase retrieval: A Green's function solution, JOSA **73**, 1434 (1983).

[30] Y. Nesterets, On the origins of decoherence and extinction contrast in phase-contrast imaging, Opt. Commun. **281**, 533 (2008).

[31] K. S. Morgan and D. M. Paganin, Applying the Fokker–Planck equation to grating-based *x*-ray phase and dark-field imaging, Sci. Rep. **9**, 17465 (2019).

[32] S. K. Lynch, V. Pai, J. Auxier, A. F. Stein, E. E. Bennett, C. K. Kemble, X. Xiao, W.-K. Lee, N. Y. Morgan, and H. H. Wen, Interpretation of dark-field contrast and particle-size selectivity in grating interferometers, Appl. Opt., AO **50**, 4310 (2011), publisher: Optical Society of America.

[33] P. Modregger, M. Kagias, S. C. Irvine, R. Brönnimann, K. Jefimovs, M. Endrizzi, and A. Olivo, Interpretation and utility of the moments of small-angle *x*-ray scattering distributions, Phys. Rev. Lett. **118**, 265501 (2017).

[34] M. Endrizzi, F. A. Vittoria, P. C. Diemoz, R. Lorenzo, R. D. Speller, U. H. Wagner, C. Rau, I. K. Robinson, and A. Olivo, Phase-contrast microscopy at high *x*-ray energy with a laboratory setup, Opt. Lett., OL **39**, 3332 (2014).

[35] C. K. Hagen, P. C. Diemoz, M. Endrizzi, and A. Olivo, The effect of the spatial sampling rate on quantitative phase information extracted from planar and tomographic edge illumination *x*-ray phase contrast images, J. Phys. D: Appl. Phys. **47**, 455401 (2014).

[36] F. A. Vittoria, M. Endrizzi, P. C. Diemoz, U. H. Wagner, C. Rau, I. K. Robinson, and A. Olivo, Virtual edge illumination and one dimensional beam tracking for absorption, refraction, and scattering retrieval, Appl. Phys. Lett. **104**, 134102 (2014).

[37] D. S. Eastwood, P. M. Bayley, H. J. Chang, O. O. Taiwo, J. Vila-Comamala, D. J. L. Brett, C. Rau, P. J. Withers, P. R. Shearing, C. P. Grey, and P. D. Lee, Three-dimensional characterization of electrodeposited lithium microstructures using synchrotron *x*-ray phase contrast imaging, Chem. Commun. **51**, 266 (2015).

[38] P. C. Diemoz, F. A. Vittoria, and A. Olivo, Spatial resolution of edge illumination *x*-ray phase-contrast imaging, Opt. Express, OE **22**, 15514 (2014).

[39] F. A. Vittoria, P. C. Diemoz, M. Endrizzi, L. Rigon, F. C. Lopez, D. Dreossi, P. R. T. Munro, and A. Olivo, Strategies for efficient and fast wave optics simulation of coded-aperture and other *x*-ray phase-contrast imaging methods, Appl. Opt., AO **52**, 6940 (2013).

[40] M. Strobl, General solution for quantitative dark-field contrast imaging with grating interferometers, Sci. Rep. **4**, 7243 (2014).

[41] S. Meyer, S. Z. Shi, N. Shapira, A. D. A. Maidment, and P. B. Noël, Quantitative analysis of speckle-based *x*-ray dark-field imaging using numerical wave-optics simulations, Sci. Rep. **11**, 16113 (2021).